

# Optimal Control of Droplets on a Solid Surface using Distributed Contact Angles

Henning Bonart<sup>a,\*</sup>, Christian Kahle<sup>b</sup>, Jens-Uwe Repke<sup>a</sup>

<sup>a</sup>*Technische Universität Berlin, Process Dynamics and Operations Group,  
Straße des 17. Juni 135, 10623 Berlin, Germany*

<sup>b</sup>*Universität Koblenz-Landau, Universitätsstraße 1, 56070 Koblenz, Germany*

---

## Abstract

Controlling the shape and position of moving and pinned droplets on a solid surface is an important feature often found in microfluidic applications. However, automating them, e.g., for high-throughput applications, does rarely involve model-based optimal control strategies. In this work, we demonstrate the optimal control of both the shape and position of a droplet sliding on an inclined surface. This basic test case is a fundamental building block in plenty of microfluidic designs. The static contact angle between the solid surface, the surrounding gas, and the liquid droplet serves as the control variable. By using several control patches, e.g., like done in electrowetting, the contact angles are allowed to vary in space and time. In computer experiments, we are able to calculate mathematically optimal contact angle distributions using gradient-based optimization. The dynamics of the droplet are described by the Cahn–Hilliard–Navier–Stokes equations. We anticipate our demonstration to be the starting point for more sophisticated optimal design and control concepts.

*Keywords:* Droplets, optimal control, contact angle, phase field model, electrowetting, lab-on-a-chip

---

## 1. Introduction

In many droplet-based microfluidic processes and applications the precise shape and position of the droplets over time play a significant role for the performance of the device. One example is the transport of droplets in a lab-on-a-chip device. Here, the droplets get merged, split and mixed at specific positions on the chip Pollack et al. (2002). Thereby, the shape of the droplets influences the

---

\*Corresponding author

*Email address:* [henning.bonart@tu-berlin.de](mailto:henning.bonart@tu-berlin.de) (Henning Bonart)

heat and mass that is exchanged with the solid surface and the surrounding fluid phase Al-Sharafi et al. (2018). A second example are optical applications where liquid droplets act as flexible lenses with continuous refraction index ranges. By adjusting their shape the curvature and hence the focal length can be precisely tuned Hou et al. (2007). In all these examples, the shape and position of the droplets (or gas-liquid interface) is regulated by adjusting the contact angles of the solid surface dynamically. However, these microfluidic devices rarely incorporate model-based optimal control strategies.

Despite the impact of optimal control in industries like aviation, automotive, and chemical, only very few articles describe optimal control within the scope of droplet-based microfluidics. In Laurain and Walker (2015) the control of the footprint and shape of a static droplet was presented. The position of a moving droplet and its shape was considered in Antil et al. (2017) in absence of gravity. Fumagalli et al. (2017) presented work on the position of the gas-liquid interface of rising liquid in a capillary. However, the simultaneous control of both the shape and position of a droplet to fulfill a target in a mathematically optimal way is absent.

Therefore, we present the surface based control of both the shape and position of droplets. The static contact angle between the solid surface, the surrounding gas and the liquid droplet serves as the control variable. The dynamics of the droplet and the gas-liquid interface are described by the Cahn–Hilliard–Navier–Stokes equations. We refer to Bonart and Kahle (2020); Bonart et al. (2019c) for a detailed description of the mathematical setup. The optimal control problem is solved using a quasi-Newton method. Gradients are derived using adjoint calculus.

The capabilities of our approach are demonstrated using two test cases: The first one is a simple but intriguing demonstration to introduce the concept. Here we consider a wetting and receding droplet on a horizontal surface. The second, more complex example is inspired by the work reported in Al-Sharafi et al. (2018), where the heat transfer into a sliding and pinned droplet is characterised, and 't Mannelje et al. (2014), where drops are trapped due to steep changes in the contact angle. We assume, that our approach and demonstration initiates further research on optimal control of droplet-based microfluidics.

The remainder of the paper is structured as follows. We discuss the control problems and our proof-of-concept in Section 2. It follows a description of the control and the optimization problem in Section 3 and the forward model in Section 4. The results of the multiple control problems including the sliding droplet are given in Section 5. A summary and conclusion is the subject of

the last section.

## 2. Description of Test Cases

To show the applicability of our approach, we consider several optimal control problems. Thereby, we always aim to optimize both the shape and position of the droplet over a given time horizon. In Section 2.1 and Section 2.2 we describe two experimental setups under consideration and in Section 2.3 we state four approaches to achieve optimal control in these settings that will be tested in this work.

### 2.1. Droplet on a Horizontal Surface

We start by revisiting one of the most simplest but still highly intriguing demonstrations of electrowetting. The simplified setup is shown in Figure 1. A single droplet is placed on a horizontal surface with an equilibrium contact angle of  $\theta_{eq} = 90^\circ$ . The solid and dashed line represent the initial and desired shape and position of the droplet. The control patches, or electrodes, below the surface are used to dynamically change the actual contact angle  $\theta$ . In this way, the spreading length of the cap-shaped droplet can be precisely adjusted. In an optical application for example this could lead to a modulation of the refractive index. A further example would be the adaptation of the heat transfer from the solid surface into the droplet. As we are not concerned here with the technical implementation of the contact angle modification we refer to the recent text book by Mugele and Heikenfeld (2018) for an extensive description.

Adjusting the voltage in the patches until the droplet reaches a specific shape and position just by trial-and-error and experience can be cumbersome. This is especially true in complex applications where inertial forces of the droplet or the surrounding phase might lead to ripples or instabilities. Therefore we do not directly specify a contact angle  $\theta$  to enforce a specific shape of the droplet. In fact, we directly incorporate the desired shape and position of the droplet into an optimal control problem. The details of this problem will be further described in Section 3.

### 2.2. Pinning a Sliding Droplet

The example above can be extended to numerous more complex applications. Exemplarily, we discuss a liquid droplet placed on an inclined solid surface. This example is inspired by the work reported in Al-Sharafi et al. (2018), where the heat transfer into a sliding and pinned droplet is

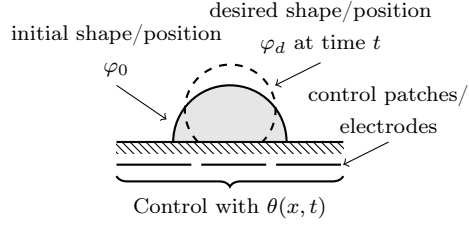


Figure 1: Illustration of the optimal control problem of the symmetric, cap-shaped droplet on a horizontal surface.

characterised, and 't Mannetje et al. (2014), where drops are trapped due to steep changes in the contact angle. Here, we want to accomplish a similar pinning of the droplet, i.e., we want to specify a desired position of the droplet. In addition, we want the droplet to have a specific shape at a specific instance in time. In Figure 2, the general physical setting of the problem is illustrated. A single droplet (solid line) is placed on an inclined surface with an equilibrium contact angle of  $\theta_{eq} = 90^\circ$ . The dashed line represents the desired shape and position at some instance in time. It is clear, that if no control action is taken, the droplet will slide down the surface driven by gravity. However, with the help of the patches  $u_1$  to  $u_4$  we want to control the advancing and receding contact angles  $\theta_1$  and  $\theta_2$  while the droplet slides along the surface. In this way, we would be able to impose the desired shape and position at a specific time  $t$  (light gray).

Apparently, it would be highly cumbersome to find control actions for the patches  $u_1$  to  $u_4$  by extensive trial-and-error. Furthermore, no guarantee can be given, that the control action based on experience would be in some sense optimal. Again we formulate an optimal control problem and incorporate the desired shape into the optimization functional.

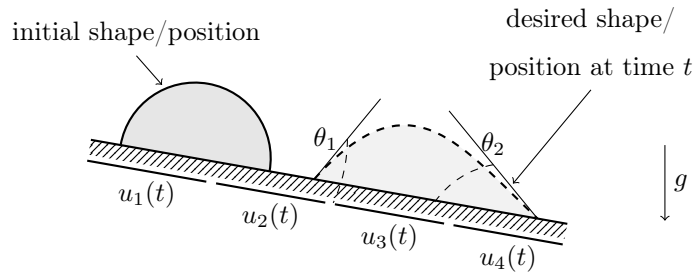


Figure 2: Physical setting of the optimal control problem.

### 2.3. Control Actions

Four different types of control actions will be discussed in this work. We start with the most simplest type and successively approach the proof-of-principle of an optimal control of both the shape and position of a droplet.

**A: Constant in Space and Time** In this setting, the control is given by one contact angle, that is constant with respect to space and time.

**B: Spatially Adapted** Here, we separate the surface into equally distributed stripes (or electrodes) and solve the optimal control problem. Each strip can feature a different but constant contact angle. Again, as the contact angles are constant in time (but not in space), we aim to calculate the optimal design of a surface.

**C: Temporal Switchable** For the next step we consider a real active control problem. That means, that this result can not be implemented in applications without some kind of active control mechanism like electrowetting. In this example, we allow the spatially homogeneous contact angle to switch at a few discrete instances in time. This correspondences to electrowetting with a single electrode.

**D: Changeable in Space and Time** Finally, we consider the most general optimal control problem. This in fact is needed to consider the sliding droplet case explained in Section 2.2. Therefore, we combine the second and third example. The surface is separated into equally distributed stripes. Each stripe is allowed to switch its contact angle at a few discrete instances in time.

In the following we consider the control actions A and B as passive controls or manufactured controls, because the control action is predefined offline by the manufacturing of the solid surface, while we call the control types C and D as active controls, as they are applied online, while the actual dynamics happens.

## 3. Construction of the Design/Control

In this section, we describe the optimization problem that we investigate to obtain optimal controls, i.e. optimal distributions of contact angles with respect to time and space. The following

modeling is independent of the actual description of the droplet. We only assume, that there is some measure to quantify the quality of a droplet with respect to some objective. We give examples at the end of this section. We also refer to our complementary works Bonart and Kahle (2020); Bonart et al. (2019c) for an extensive description of the mathematical details.

We assume, that we can influence the contact angle at the contact line with a suitable control mechanism (i.e., electrowetting). To state the optimal control problem that defines our controller, we assume, that we have some general description  $\varphi$  of the droplet. Moreover, we have some abstract control variable  $u$  together with an embedding operator  $B$  such that  $Bu$  models the actual applied distribution of contact angles in space and time. We finally assume, that for any control  $u$  we can calculate a droplet  $\varphi(u)$  utilizing some kind of forward model. The considered optimal control problem is given as

$$\begin{aligned} \min_{\varphi, u} J(\varphi, u) &= \frac{1}{2} \int_0^T \int_{\Omega} \omega(t) |\varphi(t, x) - \varphi_d(t, x)|^2 \, dx \, dt + \frac{\alpha}{2} \int_0^T \int_{\partial\Omega} |(Bu)(t, x)|^2 \, dx \, dt \\ &\text{subject to } \varphi = \varphi(u), \\ &\cos \theta_{\max} \leq Bu + \cos(\theta_{eq}) \leq \cos \theta_{\min}, \end{aligned} \tag{P}$$

where  $\varphi_d$  represent the desired shape and position of the droplet,  $\alpha > 0$  denotes a chosen regularization parameter and  $\theta_{eq}$  is the equilibrium contact angle of the solid surface without any control action. The actual objective that we encode in the first addend of  $J$  is the tracking of a given evolution  $\varphi_d$  over the time horizon  $[0, T]$  in the least-squares sense by minimizing their mismatch. We additionally add a time depending weight  $\omega(t) \geq 0$  that can be used to pronounce the mismatch in some parts of the time horizon. The second addend penalises strong control actions and can be used to minimize the controller energy. The angles  $0 < \theta_{\min} < \theta_{\max} < \pi$  are given minimum and maximum contact angles. Note that cosine is monotonically decreasing in this range, which leads to the unexpected direction of the inequalities. This can encode physical restrictions, i.e., the contact angle can not be negative, or technical issues, i.e., the control system or technique can not reach contact angles above a certain value. We have chosen this constraint to closely resemble the Young-Lippmann equation for basic electrowetting Mugele and Heikenfeld (2018). For example, if electrowetting is applied to manipulate the contact angle, the maximum accessible contact angle is equal to the equilibrium contact angle. Note, that the precise form of this objective  $J$  is not important for the conceptual approach and one might use other models to quantify the quality of a given droplet or include further restrictions. For a general introduction into the field of optimization

with constraints given by partial differential equations we refer to Hinze et al. (2009); Tröltzsch (2005).

### 3.1. Model for Control Action $u$

We model the control  $Bu$  by a linear combination of fixed and given control actions. Here the control variable  $u = (u_{rs})_{r=1, \dots, R}^{s=1, \dots, S}$  represents the amplitudes of  $R$  given control actions  $(g_r(t))_{r=1}^R$  that purely depend on time and  $S$  control actions  $(f_s(x))_{s=1}^S$  that purely depend on space. We use the model

$$(Bu)(t, x) = \sum_{r=1}^R \sum_{s=1}^S u_{rs} g_r(t) f_s(x).$$

In this way we can describe the four settings (A–D) under consideration stated in Section 2.3. To model the setting A we use  $R = 1$ ,  $g_1(t) = 1$ , and  $S = 1$ ,  $f_1(x) = 1$ , such that  $Bu(t, x) = u_{11}$  describes a constant contact angle in time and space. For the setting B, i.e. controls that depend on space, but that are constant in time, we use  $R = 1$ ,  $g_1(t) = 1$  and  $S \geq 1$ , while the setting C, i.e. the same contact angle on the whole boundary, that might change over time, we use  $R \geq 1$  and  $S = 1$ ,  $f_1(x) = 1$ . Finally, for setting D we use  $R \geq 1$  and  $S \geq 1$ . Moreover, we only consider controls, that are piecewise constant with respect to time and space, respectively. Thus if we use  $S$  controls over the time horizon  $T$ , we use  $g_s(t) = \chi_{I_s}$ . Here,  $\chi_{I_s}$  denotes the characteristic function of the interval  $I_s = (\frac{s-1}{S}T, \frac{s}{S}T]$ , i.e.  $\chi_{I_s}(t) = 1$  if  $t \in I_s$  and  $\chi_{I_s}(t) = 0$  if  $t \notin I_s$ . The same structure is used with respect to space.

### 3.2. Description of the Droplet $\varphi$

Let us finally comment on some possible ways to describe the droplet. For an in-depth description of available methods we refer to Wörner (2012). In interface tracking methods, the droplet is numerically defined by an explicit description of the interface between gas and liquid. Here one might construct a characteristic (or indicator) function for the droplet out of this description and consider this function as  $\varphi$  in the sense of (P). Such a characteristic function is directly given by volume-of-fluid methods. If a level-set method is used, we also suggest to create a corresponding characteristic function. In other case, the level-set-functions for  $\varphi$  and  $\varphi_d$  need sufficient normalization such that the mismatch  $|\varphi - \varphi_d|$  is sufficiently localized in that region where the droplets that are described by  $\varphi$  and  $\varphi_d$  are different. In phase field method, the droplet is described by a

smooth indicator function similar to a characteristic function that can directly be used in (P). We use the latter method in this work and give a brief introduction in the next section.

#### 4. Forward Model

In this section, we introduce the model for the evolution of the droplet that is used throughout this work. We consider a phase field model, coupling the incompressible Navier–Stokes equations with the Cahn–Hilliard equation, see Abels et al. (2012); Jacqmin (2000); Qian et al. (2006). Compared to sharp interface methods, phase field methods replace the infinitely thin layer (interface) between gas and liquid by a transition region with positive thickness. Moreover, they describe the distribution of the different fluids by a smooth indicator function (phase field) and do not explicitly involve the location of the transition region. It follows, that all physical properties like density or viscosity vary continuously across the interface and can be described in terms of the phase field.

Especially, the Cahn–Hilliard equation allows the contact line to move naturally on the solid surface due to a diffusive flux across the interface even if no-slip is assumed Jacqmin (2000). As summarized in the review by Wörner (2012), the Cahn–Hilliard–Navier–Stokes (CHNS) equations can easily handle topological changes of the interface (merging and breakup) Anderson et al. (1998), the contact line can be accurately represented Seppacher (1996) and the interface is implicitly tracked without any prior knowledge of the position. Furthermore, one of the major advantages is, that the formulation of the surface tension force in the Navier–Stokes (NS) equation exactly conserves both the surface tension energy and kinetic energy. This can reduce spurious currents, which are purely artificial velocities around the interface, to the level of the truncation error even for low Capillary numbers He and Kasagi (2008); Jamshidi et al. (2018).

The liquid droplet and the surrounding air are modeled as Newtonian, isotherm, immiscible and incompressible fluids. In this work, the common incompressible, single-field Navier–Stokes (NS) equation is combined with the convective Cahn–Hilliard (CH) equation to describe the interface dynamics and we use the model from Abels et al. (2012) for the bulk dynamics. To describe the spatial distribution of the two phases (liquid and gas), and thus the diffuse interface between them,



with a single variable, an order parameter or phase field  $\varphi$  is introduced as

$$\varphi(x, t) = u_l - u_g = \begin{cases} -1 & \text{for pure phase 1 or } u_l = 0, \\ +1 & \text{for pure phase 2 or } u_l = 1, \end{cases}$$

in which  $u_g$  and  $u_l$  with  $u_l + u_g = 1$  are the volume fractions of phase 1, in the following called *gas* and phase 2, in the following called *liquid*. Note that this method postulates the existence of a diffuse interface between the two phases where both phases are present. In this region both  $u_l \neq 0$  and  $u_g \neq 0$  holds and thus  $\varphi \in (-1, 1)$ . Since  $\varphi$  is assumed to be continuous across the diffuse interface, in practice we can interpret its zero-level line as a sharp separation line between gas and liquid and use this line to present numerical results. The further primal variables are given by the velocity field  $v$ , the pressure field  $p$ , and the chemical potential  $\mu$ . In this work the thermodynamically consistent diffuse interface model for large density differences between gas and liquid proposed in Abels et al. (2012) is applied

$$\rho \partial_t v + (\rho v + J) \nabla v - \operatorname{div}(2\eta Dv) + \nabla p = -\varphi \nabla \mu + \rho g, \quad (1)$$

$$-\operatorname{div}(v) = 0, \quad (2)$$

$$\partial_t \varphi + v \nabla \varphi - b \Delta \mu = 0, \quad (3)$$

$$-\sigma \epsilon \Delta \varphi + \frac{\sigma}{\epsilon} W'(\varphi) = \mu, \quad (4)$$

which is closed with the initial data and boundary conditions, compare Grün et al. (2016); Qian et al. (2006),

$$v(t=0) = v_0, \quad v = 0, \quad (5)$$

$$\varphi(t=0) = \varphi_0, \quad \sigma \epsilon \nabla \varphi \cdot \nu_\Omega + \gamma'_u(\varphi) = 0, \quad (6)$$

$$\nabla \mu \cdot \nu_\Omega = 0, \quad (7)$$

where  $\nu_\Omega$  denotes the outer unit normal on the computational domain. We use the abbreviations  $J := -b \frac{\partial \rho}{\partial \varphi} \nabla \mu$ , where  $b$  denotes the constant mobility in the Cahn–Hilliard model, and  $2Dv := \nabla v + (\nabla v)^t$ . The gravitational acceleration is denoted by  $g$  and  $p = p^{phys} - \mu \varphi$  is a shifted pressure, where  $p^{phys}$  denotes the physical pressure. The density function is denoted by  $\rho \equiv \rho(\varphi) > 0$  and satisfies  $\rho(-1) = \rho_g$  and  $\rho(1) = \rho_l$ , with  $\rho_g, \rho_l$  denoting the constant densities of the two involved fluids, i.e. gas and liquid. It is a linear function with respect to  $\varphi$ . The viscosity function is

$\eta \equiv \eta(\varphi) > 0$  and satisfies  $\eta(-1) = \eta_g$  and  $\eta(1) = \eta_l$ , with  $\eta_g, \eta_l$  denoting the viscosities of the involved fluids. Here,  $\rho$  and  $\eta$  are given by

$$\rho(\varphi) := \frac{\rho_l + \rho_g}{2} + \frac{\rho_l - \rho_g}{2}\varphi, \quad \eta(\varphi) := \frac{\eta_l + \eta_g}{2} + \frac{\eta_l - \eta_g}{2}\varphi.$$

The function  $W(\varphi)$  denotes a dimensionless potential of double-well type. Here, we choose

$$W(\varphi) := \begin{cases} \frac{1}{4}(1 - \varphi^2)^2 & \text{if } |\varphi| \leq 1, \\ (|\varphi| - 1)^2 & \text{else.} \end{cases} \quad (8)$$

The constant  $\sigma = c_W \sigma_{lg}$  denotes the surface tension between liquid and gas, where  $\sigma_{lg}$  denotes the physical value of the surface tension and the constant  $c_W$  is a necessary scaling of the physical surface tension that appears from the diffuse interface approach. For the potential (8)  $c_W$  is given by  $c_W = \frac{3}{2\sqrt{2}}$ , compare Bonart et al. (2019b). The constant  $\epsilon$  is proportional to the thickness of the diffuse transition zone between gas and liquid. For  $\epsilon \rightarrow 0$ , i.e. if the transition zone between gas and liquid becomes small, at least formally a consistent sharp interface model can be recovered, see Abels et al. (2012); Xu et al. (2018).

Finally, the contact line energy is denoted by  $\gamma$  and interpolates smoothly between the solid-liquid and solid-gas surface energies. The expression for  $\gamma$  is given by

$$\gamma_u(\varphi) = \frac{\sigma_{sl} + \sigma_{sg}}{2} + \sigma_{gl}(\cos \theta_{eq} + Bu)\vartheta(\varphi) \quad (9)$$

where  $\vartheta$  is a smooth monotonically increasing function with  $\vartheta(-1) = -\frac{1}{2}$  and  $\vartheta(1) = \frac{1}{2}$  such that  $\gamma_u(-1) = \frac{1}{2}(\sigma_{sl} + \sigma_{sg} - \sigma_{gl}(\cos \theta_{eq} + Bu)) = \sigma_{sg}$  is satisfied by Young's law, i.e.  $\sigma_{sl} - \sigma_{sg} = \sigma_{lg}(\cos \theta_{eq} + Bu)$ , and  $\gamma_u(1) = \sigma_{sl}$  holds by the same arguments. Here  $\theta_{eq}$  denotes the static equilibrium contact angle between the solid and the interface and is measured in the liquid phase, while  $\sigma_{sg}$  denotes the surface tension between solid and gas, and  $\sigma_{sl}$  denotes the surface tension between solid and liquid. Further,  $Bu$  denotes some change of the contact angle due to the applied control, see Section 3.1 for information on  $u$  and  $B$ . Note the close resemblance of our formulation of (9) and the Young-Lippmann equation for basic electrowetting Mugele and Heikenfeld (2018). It follows, that the calculated controls  $u$  can be readily implemented in electrowetting devices.

Finally we note, that an expression for  $\vartheta$  can for example be derived based on the assumption of equipartition of energy, i.e.,  $\frac{\epsilon}{2}|\nabla\varphi|^2 \approx \frac{1}{\epsilon}W(\varphi)$  Ding and Spelt (2008). This leads to  $\vartheta'(\varphi) = c_W \sqrt{2W(\varphi)}$ .

For further details about the model as well as different potentials and contact line energies we refer to Bonart et al. (2019b). For applications of the model to rising bubbles see Aland and Voigt (2012); Bonart et al. (2019b), to the pinning of droplets see Bonart et al. (2019a) and to thin liquid films see Bonart and Repke (2018). Especially for a comparison with sharp interface simulations and experimental measurements without contact line motion, see Aland et al. (2013).

The model (1)–(4) can be derived purely from thermodynamic principles Abels et al. (2012); Qian et al. (2006). Here it is postulated, that the system in the whole domain  $\Omega$  with boundary  $\partial\Omega$  can be described by the following sum of kinetic energy and Helmholtz free energy functional of Ginzburg–Landau type Jacqmin (1999)

$$E = \frac{1}{2} \int_{\Omega} \rho |v|^2 \, dx + \sigma \int_{\Omega} \epsilon^{-1} W(\varphi) + \epsilon |\nabla \varphi|^2 \, dx + \int_{\partial\Omega} \gamma \, ds. \quad (10)$$

#### 4.1. The discrete scheme

The Cahn–Hilliard–Navier–Stokes equations form a very tightly coupled and nonlinear system of four partial differential equations. Furthermore, the Cahn–Hilliard equation (3)–(4) involves fourth-order derivatives with respect to  $\varphi$ . Compared to the Navier–Stokes equation (1)–(2), which involve only second-order derivatives, this complicates the numerical treatment Wörner (2012).

For a practical implementation in a finite element scheme we introduce a time grid  $0 = t_0 < t_1 < \dots < t_{m-1} < t_m < \dots < t_M = T$  on  $I = [0, T]$  with (not necessarily) equidistant step size  $\tau > 0$ . We further introduce a triangulation  $\mathcal{T}_h$  of the domain into cells  $T_i$ , such that  $\mathcal{T}_h = \bigcup_{i=1}^N T_i$  covers the domain. On  $\mathcal{T}_h$  we introduce piecewise linear Lagrangian finite elements  $V_1 = \mathcal{P}_1$  for  $\varphi_h$ ,  $\mu_h$  and  $p_h$  and the triangular/tetrahedral Mini element  $V_2 = \mathcal{P}_1 \oplus \mathcal{B}_{1+d}$ , denoting the space of linear polynomials enriched by a cubic/quartic bubble function, for  $v_h$ . For the derivation of the weak form as well as the proof of energy stability and thermodynamic consistency we refer to Bonart et al. (2019b).

With respect to time, we consider a time-stepping scheme and state the system that we solve on one time instance. Given  $\varphi^{m-1} \in V_1$ ,  $\mu^{m-1} \in V_1$ , and  $v^{m-1} \in V_2$ , find  $\varphi_h^m \in V_1$ ,  $\mu_h^m \in V_1$ ,  $p_h^m \in V_1$

and  $v_h^m \in V_2$ , such that for all  $w \in V_2$ ,  $q \in V_1$ ,  $\Psi \in V_1$ , and  $\Phi \in V_1$  the following equations hold

$$\begin{aligned} & \frac{1}{\tau} \left( \frac{\rho^m + \rho^{m-1}}{2} v_h^m - \rho^{m-1} v^{m-1}, w \right) \\ & + a(\rho^{m-1} v^{m-1} + J^m, v_h^m, w) + (2\eta^m Dv_h^m, Dw) - (\operatorname{div} w, p_h^m) \\ & + (\varphi^{m-1} \nabla \mu_h^m, w) - (g\rho^m, w) = 0, \end{aligned} \quad (11)$$

$$-(\operatorname{div} v_h^m, q) = 0, \quad (12)$$

$$\frac{1}{\tau} (\varphi_h^m - \varphi^{m-1}, \Psi) - (\varphi^{m-1} v^{m-1}, \nabla \Psi) + \frac{\tau}{\rho_{\min}} (|\varphi^{m-1}|^2 \nabla \mu_h^m, \nabla \Psi) + (\nabla \mu_h^m, \nabla \Psi) = 0, \quad (13)$$

$$\begin{aligned} & \sigma \epsilon (\nabla \varphi_h^m, \nabla \Phi) + \frac{\sigma}{\epsilon} (W'_+(\varphi_h^m) + W'_-(\varphi^{m-1}), \Phi) - (\mu_h^m, \Phi) \\ & + \left( \frac{S_\gamma}{2} (\varphi_h^m - \varphi^{m-1}) + \gamma'_u(\varphi^{m-1}), \Phi \right)_{\partial\Omega} = 0, \end{aligned} \quad (14)$$

with  $J^m := -\frac{\partial \rho}{\partial \varphi}(\varphi^m) \nabla \mu_h^m$ ,  $\rho^m := \rho(\varphi_h^m)$ ,  $\rho^{m-1} := \rho(\varphi^{m-1})$ ,  $\eta^m := \eta(\varphi_h^m)$ , and  $\eta^{m-1} := \eta(\varphi^{m-1})$ . The contact line energy  $\gamma'_u(\varphi^{m-1})$  is given by  $\gamma'_u(\varphi^{m-1}) = \sigma_{lg}(\cos(\theta_{eq}) + B^m u) \vartheta'(\varphi^{m-1})$ , with  $B^m u := \frac{1}{\tau} \int_{t_{m-1}}^{t_m} (Bu)(t) dt$ .

One can show, that (11)–(14) admits a unique solution on every time instance, see Bonart and Kahle (2020). Especially, for every  $u$  there exist unique sequences  $(v_h^m, p_h^m, \varphi_h^m, \mu_h^m)_{m=1}^M$  that solve (11)–(14) for every  $m = 1, \dots, M$  and that is bounded by the initial data  $v_0$  and  $\varphi_0$ .

Finally, for a sequence  $(\varphi_h^m)_{m=1}^M$  we introduce the function  $\varphi_\tau$  as piecewise constant with respect to time, i.e.  $\varphi_\tau(t) \equiv \varphi_h^m$  for all  $t \in (t_{m-1}, t_m)$ .

Since  $\varphi_\tau$  in fact is a fully discrete function, we can now state (P) as

$$\min J(\varphi_\tau, u) = \sum_{m=1}^M \tau \omega^m \|\varphi_h^m - \varphi_d^m\|_{L^2(\Omega)}^2 + \frac{\alpha}{2} \sum_{m=1}^M \tau \|B^m u\|_{L^2(\partial\Omega)}^2, \quad (\text{P}_h)$$

where  $B^m u = \frac{1}{\tau} \int_{t_{m-1}}^{t_m} Bu(t) dt$ ,  $\varphi_d^m = \frac{1}{\tau} \int_{t_{m-1}}^{t_m} \varphi_d(t) dt$ , and  $\omega^m = \frac{1}{\tau} \int_{t_{m-1}}^{t_m} \omega(t) dt$  holds.

#### 4.2. Numerical Implementation

The adjoint and the gradient for (P<sub>h</sub>) are derived using standard methods and follow directly from the discrete forward model and the functional, see Bonart and Kahle (2020); Garcke, H. et al. (2019). For details on the adjoint method for optimization with partial differential equations as constraints see Hinze et al. (2009); Tröltzsch (2005). We implement the solution scheme for the forward and adjoint model as well as the gradient in Python3 using FEniCS 2019.1.0 Alnæs et al.

$l_d/\text{mm}$	$\sigma_{gl}/\text{mN m}^{-1}$	$\rho_l/\text{kg m}^{-3}$	$\eta_l/\text{mPa s}$	$\rho_g/\text{kg m}^{-3}$	$\eta_g/\text{mPa s}$	$g/\text{m s}^{-2}$	$\theta_{eq}/^\circ$
5	72.86	998	1.0	1.2	0.018	9.81	90
$\epsilon/\text{mm}$	$b/\text{m}^3 \text{J}^{-1} \text{mm}^2 \text{s}^{-1}$	$\tau/\text{s}$	$h_{min}/\text{mm}$				
0.2	0.04	0.001	0.04				

Table 1: Physical and numerical parameters of droplet (water), surrounding gas (air) and solid surface.

(2015); Logg et al. (2012). For the solution of the arising linear systems and subsystems the software suite PETSc 3.8.4 Balay et al. (2018a,b, 1997) is applied. The software IPOPT Wächter and Biegler (2006) is applied for the solution of the optimization problem.

## 5. Optimal Control of Droplets

In this section we demonstrate the applicability of our approach and framework. At first, the general setup is described. Then we describe the results for the design cases A and B as well as the active control cases C and D. Finally, we extend the first example to sliding droplets. Especially, for the pinning of the sliding droplet the most complex case D with its spatial and temporally varying contact angles is vital.

### 5.1. General Setup

Table 1 states the physical and numerical parameters applied throughout this section. Exemplarily, we used a water droplet with a diameter  $l_d = 5 \text{ mm}$  surrounded by air on a solid surface with  $\theta_{eq} = 90^\circ$ . The time step was set to  $\tau = 0.001 \text{ s}$ . An adaptive mesh was utilized so that the interface between gas and liquid was resolved with at least four cells at all times ( $h_{min} = 0.04 \text{ mm}$ ).

The desired shapes  $\varphi_d$  were created by simulating the forward model (11)–(14) from a suitable initial value, which is specified for the individual setups, until the equilibrium droplet shape was reached.

The values of  $R$  and  $S$  for the four control cases described in Section 2 are given in Table 2 for the two numerical examples presented in Section 5.2 and Section 5.3. In both examples the stripes as well as the switching points were equally distributed over the length of the bottom wall and the time horizon of  $I = [0.0, T]$  with  $T = 1 \text{ s}$ , respectively, compare Section 3.1.

	Prob. 1				Prob. 2
	A	B	C	D	D
R	1	1	5	5	10
S	1	5	1	5	10

Table 2: Values of  $R$  and  $S$  for the control cases A to D for both problems described in Section 2.

The weight  $\omega$  was chosen as

$$\omega(t) = \begin{cases} 1 & \text{if } t \in (0, 0.8)\text{s}, \\ 10^5 & \text{if } t \in [0.8, 1.0]\text{s}, \end{cases}$$

to promote a good matching of  $\varphi$  and  $\varphi_d$  at the end of the optimization horizon between 0.8s and 1.0s. We stopped the optimizer as soon as the initial gradient  $\nabla J$  was reduced by a factor of  $\frac{1}{100}$ .

### 5.2. Droplet on a Horizontal Surface

At first, we report on the optimal control of the first example described in Section 2. The domain was of dimension  $\Omega = l_d \times l_d$  and we made use of the symmetrical droplet. In this way, we assumed symmetric conditions at the left side of the domain and solid walls at the top, bottom and right side of the domain. The bottom wall contained the control of the contact angle. The desired shape  $\varphi_d$  with an equilibrium contact angle of  $135^\circ$  is shown as the dashed line in Figure 3. In the first row of Figure 3 the initial droplets with  $Bu = 0$  and  $\theta_{eq} = 90^\circ$  are shown. The values for  $R$  and  $S$  for the control cases described in Section 2 are given in Table 2. In this example, at most five stripes with each five switching points in time were considered.

We discuss the following aspects of our numerical results:

*Resulting Droplet Shapes.* The droplet shapes calculated with the resulting optimal control values  $Bu$  for the cases A to D are depicted in Figure 3. The solid lines represent the isolines where  $\varphi = 0$ . We show the shape and position of the droplet at five instances in time. Note, that only the relevant clipping of  $\Omega$  is displayed in Figure 3.

*Relative Mismatch.* The relative mismatch between the actual droplet and the desired shape over time,

$$\frac{\Delta\varphi(t)}{\Delta\varphi^0} = \sqrt{\frac{\int_{\Omega}(\varphi(t) - \varphi_d)^2 \, dx}{\int_{\Omega}(\varphi^0 - \varphi_d)^2 \, dx}} \, , \quad (15)$$

which is normalized with the mismatch at  $t = 0.0$  s, is displayed in the top part of Figure 5.

*Optimal Controls.* The corresponding optimal controls  $Bu$  for the cases A to D are plotted in Figure 4. In the first two columns the controls are constant in time, whereas the controls are constant in space in the first and third column. The dashed lines represent the control which was used to create the desired shape  $\varphi_d$  (i.e.,  $\cos(135^\circ) \approx -0.7071$ ).

*Relative Controller Strength.* The relative controller strength per time interval  $r$  is calculated with

$$\frac{E_r}{E_A} = \frac{\frac{1}{S} \sqrt{\sum_{s=1}^S u_{rs}^2}}{|u_A|} \, . \quad (16)$$

The control strength per time interval is normalized to the (constant) control strength needed in case A. We further assume, that the control costs scale linearly with the length of the control domain, which leads to the normalization with  $\frac{1}{S}$  in the numerator. It is plotted in the lower part of Figure 5.

### 5.2.1. Cases A and B

Comparing the design cases A and B (first and second column in Figure 3 it is evident that the droplet behave almost identical: the shapes and the positions of the contact lines are very similar. The desired shape is reached with very high accuracy after a short time (see  $t = 0.4$  s) in both cases. The mismatches  $\Delta\varphi$  displayed in the top part of Figure 5 (solid lines with triangular and circular markers) decline with the same slope over time and reach almost zero at around  $t = 0.4$  s.

Now we focus on the first and second column of Figure 4 to include the optimal controls into our discussion. In case A we only allowed for a single control action for the whole surface and time horizon. Subsequently, only one value is displayed in column one. As expected from the shape of the droplet, the control value is very close to the value which was used to create the desired droplet  $\varphi_d$ , see the dashed line in the lower left panel of Figure 4.

In case B the stripe between 2 mm and 3 mm has a control value which is slightly lower than the equilibrium value obtained again in the stripe  $[1, 2]$  mm. This results in a more rapid receding of

the droplet on that stripe in case B. However, as the droplet spends only little time on that stripe the influence on the overall dynamics of the droplet are low. Since in case B only a portion of the bottom controls are active at any time, the controller strength is significantly lower compared to case A, see the lower part of Figure 5.

### 5.2.2. Cases C and D

From comparing the shape of the droplets in the active cases C and D (third and fourth column in Figure 3 we again notice that the droplets behave almost identical: the shapes and the positions of the contact lines are very similar. The desired shape is reached relatively late but still a very high accuracy after  $t = 0.8$  s in both cases. This stems from the weight  $\omega$  defined above, which was strongly penalizing the interval  $[0.8, 1.0]$ . Before 0.6 s the droplets do not move at all. This can be seen by looking at the mismatches of  $\varphi$  displayed in the top part of Figure 5 (solid lines with rectangular and open circular markers). Until 0.6 s the mismatch gets even higher than the initial mismatch. This is due to the initial droplet adapting to gravity. The subsequent decline however is very rapid and happens with almost the same slope over time for the cases C and D. Finally, it reaches a small value at around  $t = 0.8$  s.

By investigating the controls in the third and fourth column of Figure 4 the explanation for the observed droplet shapes becomes obvious. In the first three intervals the control action is approximately zero. Only for the last intervals control actions are needed to reach the desired shape in time. This leads to very low relative controller strengths required to reach the optimization target, see the lower panel of Figure 5. The most complex control sequence is calculated in case D. Here, the droplet moves in a very versatile and controlled fashion until it reaches the desired shape with a very low relative controller strength.

For all cases A to D we were able to calculate optimal controls to reach the desired shape for a specific time interval: the shapes of the droplets match the desired shape in all cases almost perfectly (Figure 3 and the mismatch gets very low (Figure 5, top). In cases C and D, the mismatch decreases slower than in cases A and B. This indicates, that a shorter time horizon would be sufficient for the control task. In all cases the final control values for the stripe between 1 mm and 2 mm is almost the same as the one used for the desired shape (Figure 4). This is expected, since the desired shape is stable situation with a constant contact angle. Moreover, the final contact point is located in this stripe, thus defining the shape of the droplet. Subsequently, the required relative controller



strengths in the cases C and D are much smaller than in the cases A and B (Figure 5, bottom). This is due to the fact, that the more complex controls can act more locally precise with respect to space and time. Thus they are not active (i.e.  $Bu = 0$ ) in large parts of the spatial and temporal domain.

### 5.3. Pinning a Sliding Droplet

To demonstrate the general applicability of our approach we extend the example discussed in Section 5.2 to the optimal pinning of a sliding droplet. The pinning of a sliding droplet at a specific position on a solid surface while maintaining a desired shape can have interesting implications for technical applications. At the same time, this is a challenging task.

The domain was of dimension  $\Omega = 2l_d \times l_d$ . We assumed symmetric conditions at the left side of the domain and solid walls at the top, bottom and right side of the domain. The inclined bottom wall contained the control of the contact angle. The inclination of the plate was  $45^\circ$  to the horizontal. Exemplary, we used the dashed line in Figure 6 as the desired shape  $\varphi_d$  at this position on the inclined surface. The desired droplet was produced by simulating the forward model from a cap-shaped droplet at  $(x, y) = (1.25l_d, 0)$  with  $Bu = -0.7071$  and  $\theta_{eq} = 90^\circ$ . In the first row of Figure 6 the initial droplets at  $t = 0$  and  $(x, y) = (0.75l_d, 0)$  with  $Bu = 0$  and  $\theta_{eq} = 90^\circ$  are shown. The values for  $R$  and  $S$  are given in Table 2. We considered ten stripes with each ten switching points in time. The stripes as well as the switching points were equally distributed over the space of 10 mm and the time horizon of 1 s.

*No Control.* At first we show the droplet sliding down the inclined surface without any control at all ( $Bu = 0$  for all times), see the first column in Figure 6. Secondly, one might naively set the control to the finally desired contact angle of  $135^\circ$ . This is displayed in the second column. In both cases the droplet is far from the desired shape as well as the desired position at the specified time. It is clearly evident that finding the right control actions by trial-and-error might be certainly cumbersome. Furthermore, we do not only want to obtain any controls but the controls which minimize the functional  $(P_h)$ .

*Optimal Control.* In the third column of Figure 6 the droplet's isolines calculated from the optimal control action are displayed. We notice, that in the optimal case we match the desired shape at the desired position very well between 0.8 s and 1.0 s. Comparing this to the naive approaches with

$Bu = 0$  and  $Bu = -0.7071$  the improvement is tremendous. During the sliding and pinning the droplet exhibits multiple surprising shapes due to the strong impact of the control actions on the droplet.

The control actions  $Bu$  in each time interval are shown in the last column of Figure 6. It is striking how complex these optimal controls  $Bu$  are. We would have found this very difficult and costly to find this control action by trial-and-error. While pulled by gravity, each of the droplet's contact points are forced to recede and spread multiple times. See for example between 0.4s and 0.6s the stripes between 1 mm to 2 mm and 7 mm to 8 mm. The control action jumps from between large and small values, which leads to the pinning of the contact points.

## 6. Conclusion

In this work we demonstrated for the first time some capabilities of optimal control of both the shape and position of a droplet. Therefore, we considered the active control of a sliding droplet using temporally and spatially varying optimal contact angle distributions. In this basic example common for droplet-based microfluidics the droplet slides on an inclined surface and gets pinned at a specific position with a desired shape. In our demonstration, the final position and shape of the droplet matched the desired properties almost perfectly. The dynamics of the droplets were calculated using a phase field model. We solved the optimal control problem using a quasi-Newton method. The Gradients were calculated using the adjoints. The resulting controls were profoundly complex and would not have been found by trial-and-error. Our work indicates that optimal control of droplets is not only possible but might enable further automation of droplet-based microfluidic devices for example in high-throughput applications. However, more in-depth research of the individual aspects of the concept, like objectives or constraints, is required. This is our subject for future work.

## Acknowledgments

The first and third author thank the German Research Foundation (DFG) for the financial support within the project RE 1705/16-1.

## References

- Abels, H., Garcke, H., and Grün, G. (2012). Thermodynamically consistent, frame indifferent diffuse interface models for incompressible two-phase flows with different densities. *Mathematical Models and Methods in Applied Sciences*, 22(3):1150013(40).
- Al-Sharafi, A., Yilbas, B. S., Ali, H., and Alaqeeli, N. (2018). A Water Droplet Pinning and Heat Transfer Characteristics on an Inclined Hydrophobic Surface. *Scientific Reports*, 8(1):3061.
- Aland, S., Boden, S., Hahn, A., Klingbeil, F., Weismann, M., and Weller, S. (2013). Quantitative comparison of Taylor Flow simulations based on sharp- and diffuse-interface models. *International Journal for Numerical Methods in Fluids*, 73(4):344–361.
- Aland, S. and Voigt, A. (2012). Benchmark computations of diffuse interface models for two-dimensional bubble dynamics. *International Journal for Numerical Methods in Fluids*, 69:747–761.
- Alnæs, M. S., Blechta, J., Hake, J., Johansson, A., Kehlet, B., Logg, A., Richardson, C., Ring, J., Rognes, M. E., and Wells, G. N. (2015). The FEniCS Project Version 1.5. *Arch. Numer. Softw.*, 3(100).
- Anderson, D. M., McFadden, G. B., and Wheeler, A. A. (1998). Diffuse-interface methods in fluid mechanics. *Annu. Rev. Fluid Mech.*, 30(1):139–165.
- Antil, H., Hintermüller, M., Nochetto, R., Surowiec, T., and Wegner, D. (2017). Finite horizon model predictive control of electrowetting on dielectric with pinning. *Interfaces and Free Boundaries*, 19(1):1–30.
- Balay, S., Abhyankar, S., Adams, M. F., Brown, J., Brune, P., Buschelman, K., Dalcin, L., Eijkhout, V., Gropp, W. D., Kaushik, D., Knepley, M. G., May, D. A., McInnes, L. C., Mills, R. T., Munson, T., Rupp, K., Sanan, P., Smith, B. F., Zampini, S., Zhang, H., and Zhang, H. (2018a). PETSc Web page. <http://www.mcs.anl.gov/petsc>.
- Balay, S., Abhyankar, S., Adams, M. F., Brown, J., Brune, P., Buschelman, K., Dalcin, L., Eijkhout, V., Gropp, W. D., Kaushik, D., Knepley, M. G., May, D. A., McInnes, L. C., Mills, R. T., Munson, T., Rupp, K., Sanan, P., Smith, B. F., Zampini, S., Zhang, H., and Zhang, H. (2018b). PETSc users manual. Technical Report ANL-95/11 - Revision 3.9, Argonne National Laboratory.

- Balay, S., Gropp, W. D., McInnes, L. C., and Smith, B. F. (1997). Efficient management of parallelism in object oriented numerical software libraries. In Arge, E., Bruaset, A. M., and Langtangen, H. P., editors, *Modern Software Tools in Scientific Computing*, pages 163–202. Birkhäuser Press.
- Bonart, H., Jung, J., Kahle, C., and Repke, J.-U. (2019a). Influence of Liquid Density and Surface Tension on the Pinning of Sliding Droplets on a Triangular Microstructure. *Chemical Engineering & Technology*, 42(7):1381–1387.
- Bonart, H. and Kahle, C. (2020). Optimal Control of Sliding Droplets using the Contact Angle Distribution. *arXiv:2002.02273*.
- Bonart, H., Kahle, C., and Repke, J.-U. (2019b). Comparison of energy stable simulation of moving contact line problems using a thermodynamically consistent Cahn–Hilliard Navier–Stokes model. *Journal of Computational Physics*, 399:108959.
- Bonart, H., Kahle, C., and Repke, J.-U. (2019c). Controlling sliding droplets with optimal contact angle distributions and a phase field model. *PAMM*, 19(1):e201900223.
- Bonart, H. and Repke, J.-U. (2018). Direct numerical simulations of liquids on microstructured surfaces: Analysing the fluid dynamics on packing. *Chem. Eng. Trans.*, 69:61–66.
- Ding, H. and Speltz, P. D. M. (2008). Onset of motion of a three-dimensional droplet on a wall in shear flow at moderate Reynolds numbers. *J. Fluid Mech.*, 599(March 2008):341–362.
- Fumagalli, I., Parolini, N., and Verani, M. (2017). Optimal control in ink-jet printing via instantaneous control. *Computers and Fluids*, 172:264–273.
- Garcke, H., Hinze, M., and Kahle, C. (2019). Optimal control of time-discrete two-phase flow driven by a diffuse-interface model. *ESAIM: COCV*, 25:13.
- Grün, G., Guillén-González, F., and Metzger, S. (2016). On Fully Decoupled Convergent Schemes for Diffuse Interface Models for Two-Phase Flow with General Mass Densities. *Communications in Computational Physics*, 19(5):1473–1502.
- He, Q. and Kasagi, N. (2008). Phase-Field simulation of small capillary-number two-phase flow in a microtube. *Fluid Dyn. Res.*, 40(7-8):497–509.

- Hinze, M., Pinnau, R., Ulbrich, M., and Ulbrich, S. (2009). *Optimization with PDE Constraints*, volume 23 of *Mathematical Modelling: Theory and Applications*. Springer Netherlands, Dordrecht.
- Hou, L., Smith, N. R., and Heikenfeld, J. (2007). Electrowetting manipulation of any optical film. *Applied Physics Letters*, 90(25):251114.
- Jacqmin, D. (1999). Calculation of Two-Phase Navier–Stokes Flows Using Phase-Field Modeling. *J. Comput. Phys.*, 155(1):96–127.
- Jacqmin, D. (2000). Contact-line dynamics of a diffuse fluid interface. *J. Fluid Mech.*, 402(2000):S0022112099006874.
- Jamshidi, F., Heimel, H., Hasert, M., Cai, X., Deutschmann, O., Marschall, H., and Wörner, M. (2018). On suitability of phase-field and algebraic volume-of-fluid OpenFOAM® solvers for gas–liquid microfluidic applications. *Comput. Phys. Commun.*
- Laurain, A. and Walker, S. W. (2015). Droplet Footprint Control. *SIAM Journal on Control and Optimization*, 53(2):771–799.
- Logg, A., Mardal, K.-A., and Wells, G., editors (2012). *Automated Solution of Differential Equations by the Finite Element Method - The FEniCS Book*, volume 84 of *Lecture Notes in Computational Science and Engineering*. Springer.
- Mugele, F. and Heikenfeld, J. (2018). *Electrowetting*. Wiley-VCH Verlag GmbH & Co. KGaA, Weinheim, Germany.
- Pollack, M. G., Shenderov, A. D., and Fair, R. B. (2002). Electrowetting-based actuation of droplets for integrated microfluidics. Electronic supplementary information (ESI) available: six videos showing droplet flow, droplet dispensing and electrowetting. See <http://www.rsc.org/suppdata/lc/b1/b110474h/>. *Lab on a Chip*, 2(2):96.
- Qian, T., Wang, X.-P., and Sheng, P. (2006). A variational approach to moving contact line hydrodynamics. *Journal of Fluid Mechanics*, 564:333–360.
- Seppecher, P. (1996). Moving contact lines in the Cahn-Hilliard theory. *Int. J. Eng. Sci.*, 34(9):977–992.

- 't Mannetje, D., Ghosh, S., Lagraauw, R., Otten, S., Pit, A., Berendsen, C., Zeegers, J., van den Ende, D., and Mugele, F. (2014). Trapping of drops by wetting defects. *Nature Communications*, 5(1):3559.
- Tröltzsch, F. (2005). *Optimale Steuerung partieller Differentialgleichungen*. Vieweg Verlag, Wiesbaden.
- Wächter, A. and Biegler, L. T. (2006). On the implementation of an interior-point filter line-search algorithm for large-scale nonlinear programming. *Mathematical programming*, 106(1):25–57.
- Wörner, M. (2012). Numerical modeling of multiphase flows in microfluidics and micro process engineering: a review of methods and applications. *Microfluid. Nanofluidics*, 12(6):841–886.
- Xu, X., Di, Y., and Yu, H. (2018). Sharp-interface limits of a phase-field model with a generalized Navier slip boundary condition for moving contact lines. *Journal of Fluid Mechanics*, 849:805–833.

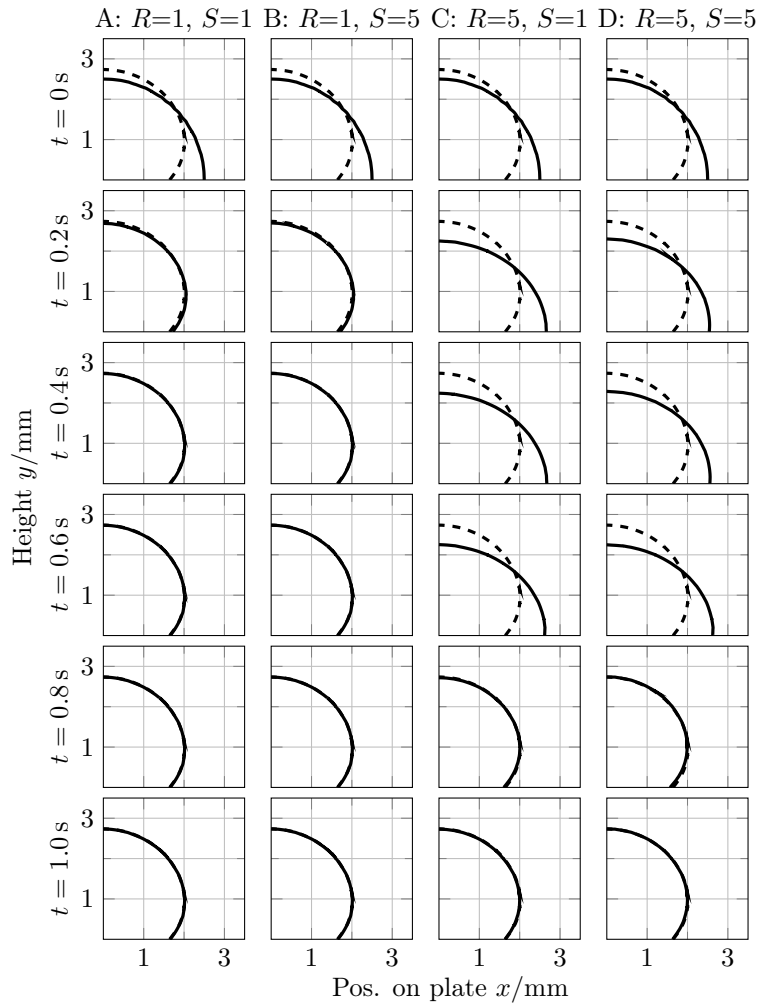


Figure 3: Development of the receding droplets over time for the optimization cases A to D. Due to the symmetric droplet only the right half of the isoline for  $\varphi = 0$  is displayed. The desired shape and position of the droplet  $\varphi_d$  is included as the dashed line.

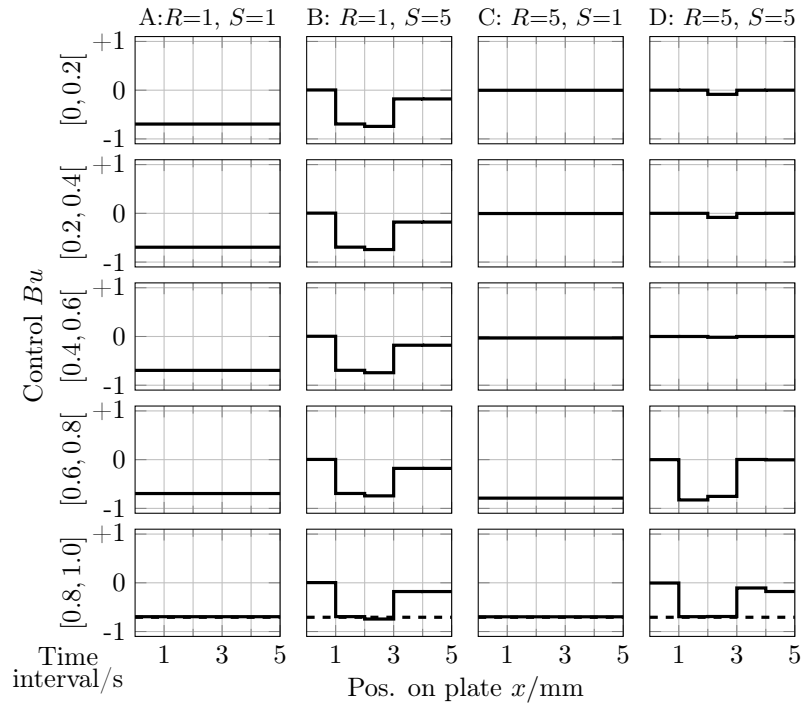


Figure 4: Development of the controls over time for the optimization cases A to D. Due to the symmetric droplet only the right half of the controls is displayed. The control which was used to create the desired droplet  $\varphi_d$  is displayed as the dashed line at the bottom row.



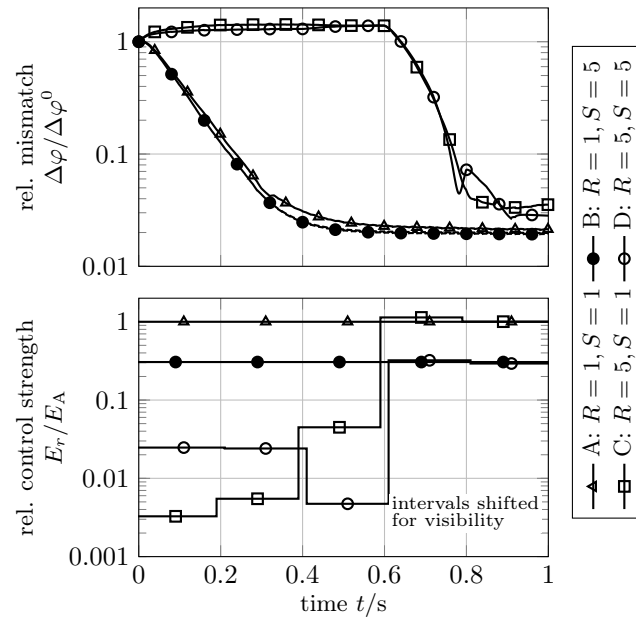


Figure 5: Development of the relative mismatch (top) and the relative control strength for the cases A, B, C and D.

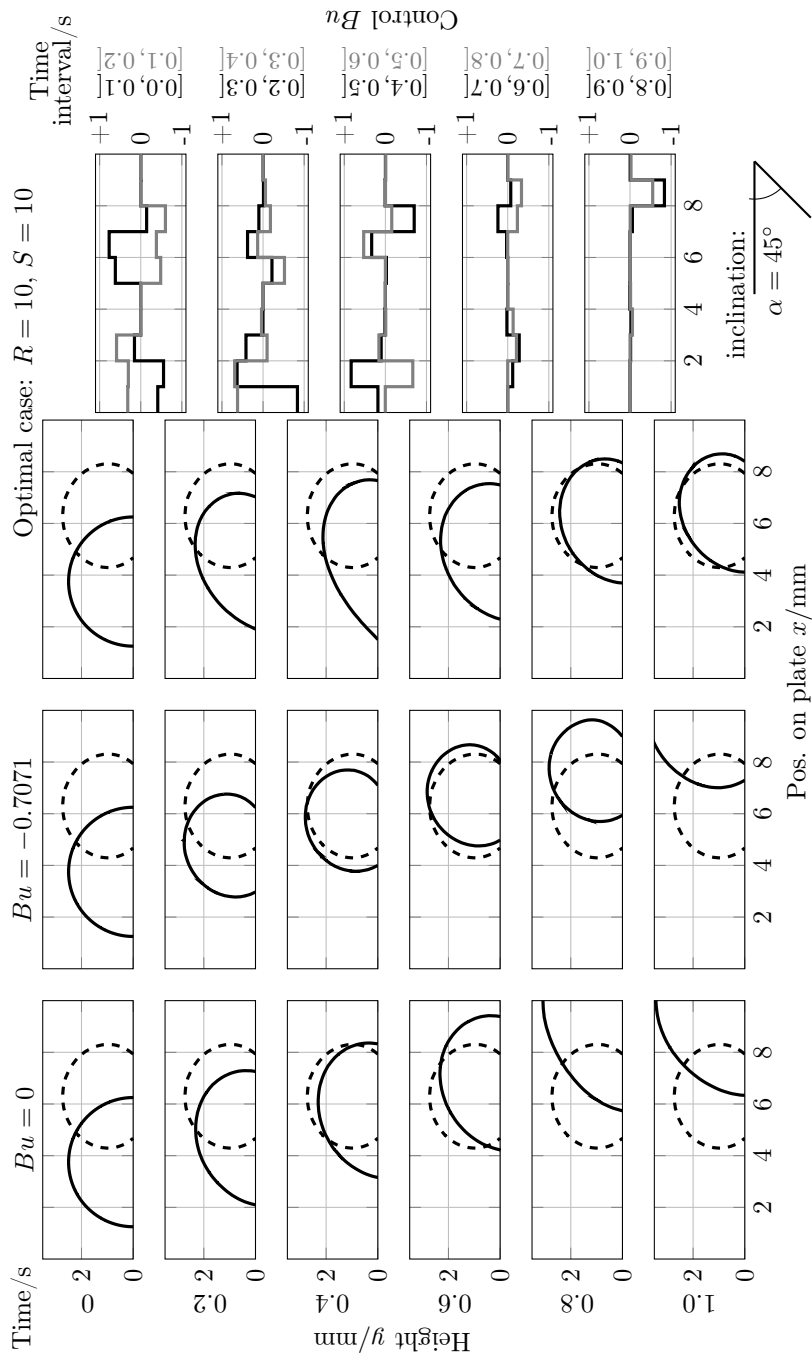


Figure 6: Development of the sliding and pinned droplets over time on a plate with an inclination to the horizontal of  $\alpha = 45^\circ$ : no control action with  $Bu = 0$  (first column), constant control action with  $Bu = -0.7071$  (second column) and optimal control action for  $R = 10$  and  $S = 10$  (third column). In the fourth column the optimal control action is displayed for the time intervals. The desired shape and position of the droplet  $\varphi_d$  is included as the dashed line.